Journal of the European Ceramic Society 41 (2021) 4302–4312

Contents lists available at ScienceDirect

Journal of the European Ceramic Society

journal homepage: www.elsevier.com/locate/jeurceramsoc

Improved thermal stability of zirconia macroporous structures via homogeneous aluminum oxide doping and nanostructuring using atomic layer deposition

Raphael J. Gehensel [a], Robert Zierold [b], Gunnar Schaan [c], Guoliang Shang [d], Alexander Yu Petrov [d], Manfred Eich [d,e], Robert Blick [b], Tobias Krekeler [c], Rolf Janssen [a], Kaline P. Furlan [a,b,*]

[a] Institute of Advanced Ceramics, Hamburg University of Technology, Denickestraße 15, 21073 Hamburg, Germany
[b] Center for Hybrid Nanostructures, Universität Hamburg, Luruper Chaussee 149, 22761 Hamburg, Germany
[c] Electron Microscopy Unit (BeEM), Hamburg University of Technology, Eißendorfer Straße 42, 21073 Hamburg, Germany
[d] Institute of Optical and Electronic Materials, Hamburg University of Technology, Eißendorfer Straße 38, 21073 Hamburg, Germany
[e] Institute of Materials Research, Helmholtz-Zentrum Geesthacht, Max-Planck-Strasse 1, 21502 Geesthacht, Germany

ARTICLE INFO

Keywords:
Ceramics
Porous materials
High-temperature applications
Inverse opals
Atomic layer deposition

ABSTRACT

Dopants are regularly used in sol-gel and powder metallurgy routes, however, the controlled insertion of such is quite challenging, especially in the case of nanostructures. Here we investigate the use of atomic layer deposition (ALD) as a potential technique to precisely introduce aluminum oxide as dopant or second phase into zirconia 3D macroporous nanostructures. The results show that the introduction of high Al_2O_3 contents into the zirconia nanostructures successfully inhibited sintering when in comparison to undoped zirconia. Moreover, for the multi-nanolaminated and full-mix structures, the tetragonal phase was stabilized up to 1200 °C. Furthermore, the structures presented a photonic band gap even after heat treatment at 1200 °C for 2 h, enabling its application as inverse opal photonic crystals in high-temperature environments. The enhancement of thermal stability and high-temperature tetragonal phase stabilization is enabled jointly by the nanostructuring and homogeneous distribution of aluminum oxide provided by ALD super-cycles.

1. Introduction

Inverse opals are highly-ordered 3D hierarchical macroporous structures which find application in a diversity of technological areas such as catalysis, sensing, electrodes, wetting, filtration and optics [1]. They are often produced by the infiltration of a colloidal crystal template with different materials, generating polymeric, metallic, and ceramic inverse opals (IOs) after the template burn-out [2–4].

One of the prospected high-temperature applications of such materials is as reflective thermal barrier coatings, where the inverse opals act as inverse opal photonic crystals. However, for the successful application, such macroporous structures need to be thermally stable and preserve their properties during and after temperature exposure. Specifically, the periodically ordered dielectric structure, often in the sub micrometer range, responsible for the reflection of electromagnetic waves and, thus, the photonic band gap, needs to be stable at the envisaged operational temperatures. However, the high temperature exposure promotes sintering and grain growth, resulting in morphological changes in the materials and even destruction of the periodic structure [5]. Furthermore, the nanosized structural features and macropores have a high surface-to-volume ratio, which can further enhance sintering as surface diffusion becomes relevant. Therefore, there is a demand in restricting sintering as a mean to promote structural stabilization.

Ceramic-based macroporous structures are attractive for applications in demanding environments, due to their enhanced chemical and thermal stability when compared to polymers or common metals. Typically, the material and the finest micro or nanostructure characteristics are determined by the infiltration process, which can be performed by a variety of methods. Infiltration by sol-gel or powder colloidal suspensions is widely used due to its simplicity [6–9], standing next to chemical vapor deposition and atomic layer deposition (ALD),

* Corresponding author at: Institute of Advanced Ceramics, Hamburg University of Technology, Denickestraße 15, 21073 Hamburg, Germany.
E-mail address: kaline.furlan@tuhh.de (K.P. Furlan).

https://doi.org/10.1016/j.jeurceramsoc.2021.02.007
Received 2 October 2020; Received in revised form 8 February 2021; Accepted 8 February 2021
Available online 11 February 2021

which provide a better control over the nanostructure due to its self-limiting nature. Low-temperature ALD is especially interesting for the infiltration polymeric templates [2,10–15]. Material wise, yttria stabilized zirconia (YSZ) [6,16] is an established ceramic material for high temperature applications, but also zirconia [17], silica [18,19], titania [2,19], alumina [20], and mullite [12], have been successfully used as high-temperature macroporous ceramics, with limit temperatures varying from 850 °C for silica up to 1400 °C for mullite [2,19].

Zirconia-based ceramics are employed in a variety of applications such as grinding media, dental implants, orthopaedical implants, catalyst support, optical fiber connectors, solid oxide fuel cells, thermal barrier coatings and high-temperature structural ceramics [21,22]. Nonetheless, pure zirconia is rarely used and partial or full stabilization of a certain crystal structure is necessary to guarantee the structural integrity of such parts during processing, and also for high-temperature applications. Pure zirconia presents two main phase transitions, from monoclinic crystal structure to tetragonal (m→t) and then to cubic (t→c). The inverse t→m transition is especially critical during the cooling stage of parts' processing, as the associated 5 % volume expansion can generate cracks or complete disintegration of the ceramic component [22]. For high-temperature applications, the phase transition would occur in the other direction, with associated shrinkage, but the outcome in terms of damage could be the same. Nonetheless, the t→m or the c→m phase transformation is widely used to increase fracture toughness of zirconia-based ceramics. In this case, the phase transformation is induced by deformation and the volume expansion is used to shield crack tips from advancing. In all cases, there is an interest in stabilization of zirconia high-temperature phases, i.e. tetragonal or cubic. Moreover, the cubic phase is highly desirable for its enhanced ionic conductivity properties [21,22].

Such stabilization is extensively explored and often achieved by yttria doping, generating partially stabilized zirconia (PSZ) or fully stabilized zirconia (YSZ) depending on the doping content, often varied between 3 and 8 mol.%. The phase to be stabilized, cubic or tetragonal, has been shown to vary depending on the yttria content [23]. Doping has also been demonstrated possible for Al, Fe, Ga, Gd, Ge, Mg, Ca, and Ce cations [21,22]. For trivalent cations, the phase stabilization is associated the charge destabilization and oxygen vacancies generation, which favors the eightfold co-ordination in the crystal lattice. For tetravalent cations, the stabilization is related to the lattice distortion caused by the cations which counteract the lattice strain caused by an eightfold co-coordination of Zr^{+4} cations. A stabilization of tetragonal phase at room temperature has also been reported for nanometric powders, which then transform to monoclinic upon heating [21,22].

Doping of certain species into a host material is also an established method to modify sintering behavior and microstructural aspects [24]. Often, the insertion of dopants distorts the crystal lattice resulting in blockage (or enhancement [25]) of diffusion pathways and could also promote grain boundary pinning, hindering grain growth [25–27]. Doping or intermixing of Al_2O_3 into zirconia, has been widely explored in the literature and several different methods such as powder metallurgy (PM) [28,29], sol–gel [30–34], pulsed laser deposition (PLD) [35,36], chemical vapor synthesis (CVS) [29] and sputtering [37–42] were used to fabricate samples. The reasons for aluminum oxide doping or additions are several and depend on the targeted application. In common powder metallurgy products, aluminum oxide (Al_2O_3) is often introduced in zirconia (ZrO_2) to hinder the t→m phase transformation at low-temperature (ageing) for biomedical applications [28,43,44] and to refine the microstructure [29,45], whilst zirconia is introduced in alumina mostly to enhance its mechanical properties (zirconia toughened alumina, ZTA) [28,46]. The increase in fracture toughness, has also been the focus of sol-gel products [47,48], but mostly to control the zirconia phases crystallization and transformation, with focus on tetragonal phase stabilization [30,31,33,34,49]. The tailoring of phases has also been the focus of reports on PLD [35,36] and sputtered coatings [37–39]. In these films, the phase stabilization is reported to be caused not only by doping and crystallize size control, but also to the constraining effects induced by the layering [35,36,39]. At such, Ghosh et al. [35] has reported that the crystallite size is restricted by the original layer thickness and even after heat treatment, present nanometer size. Meanwhile, studies by the group of Gajdardziska–Josifovska have demonstrated that the volume fraction of tetragonal phase increases with decreasing zirconia layer thickness [37].

The controlled insertion of dopants into the submicrometric to nanometric structures, such as inverse opals, is yet a huge challenge. Sol-gel routes often are limited in the capability of high-content doping, as segregation [50] or precipitation of undesired monophasic phases due to different precursor reactivity [15,51,52] is prone to occur. Furthermore, sol-gel films or sol-gel infiltrated structures need a drying step for solvent removal, in which cracks are generated [15,51,52]. Meanwhile, the already-reported deposition processes have limits in relation to infiltration of the three dimensional macroporous structures, as they are based on physical deposition. Alternatively, ALD offers an outstanding capability to tailor the nanostructure and the material of which, including doping, with thickness control down to angstrom size and stable chemical reactions [53–55]. In ALD-based coatings, doping or intermixing of materials can be realized by super-cycling of binary ALD processes, for which the low-temperature infiltration of high-aspect ratio polymeric-based photonic crystals' templates with mullite (Al_2O_3:SiO_2) has been already demonstrated possible by our group [12]. Moreover, the ALD deposition of planar Al_2O_3-ZrO_2 films has already been explored for the fabrication of permeation barriers for oxygen and moisture in the encapsulation of OLEDs [53,54,56,57], thereby being suitable binary processes for ALD super-cycling. For our specific application, namely photonic crystals, the choice of these materials is based on two aspects. First, the reflectance capability of photonic crystals is dependent, among other factors, on the refractive index of the structure in relation to the surrounding media (air in our case). While Al_2O_3 ALD films are reported to have refractive indexes around 1.65 (@632 nm of wavelength) [13], zirconia ALD films are reported to have much higher values, reaching up to 2.10 @633 nm of wavelength [58]. Thereby, there is an interest on using zirconia as the shell material in inverse opal photonic crystals. Nonetheless, zirconia materials only find applicability if there is a control and stability in the crystal structure, as previously discussed, so the second aspect is the need for doping. The choice for alumina over yttria is based simply on the fact that the precursors available to deposit yttria need very high temperatures for evaporation (190 °C in the former report by Shim et al. [59]) and thereby, not suitable for deposition onto polymeric templates as the low chamber temperature would be a cold spot for such precursors resulting in precursor recondensation and eventually CVD. Meanwhile, aluminum oxide ALD is a very stable process and the infiltration of polymeric templates is possible even at low temperatures, as already demonstrated by our group [12]. Moreover, alumina is well known in powder metallurgy community as a high-temperature stable material.

In this work, ALD was used to fabricate ceramic-based macroporous inverse opals' structures for high-temperature applications. By ALD it was possible to introduce tailored doping of aluminum oxide into zirconia, as well as the generation of dual and multilayered nanostructures, with an aluminum oxide content ranging from 1 to 43 wt.%. The influence of the ALD-super-cycle-based doping and nanostructuring on the sintering behavior thermal stability of zirconia macroporous structures was investigated. The phase transformations and morphological changes due to heat treatment were assessed by X-ray diffraction (XRD) and scanning electron microscopy (SEM), and evaluated according to the dopant content and nanostructuring. The tailored introduction of Al_2O_3 into the zirconia nanostructures successfully stabilized the tetragonal phase up to 1200 °C, beyond that of earlier reports, whilst inhibiting sintering, thereby minimizing the morphological changes of the inverse opals (IO). The best results for our targeted application as inverse opal photonic crystals (iPhCs) were achieved in nanostructured iPhCs, which presented a thermal stability outperforming the base zirconia iPhC, thus

presenting a photonic band-gap even after exposure at 1200 °C for 2 h.

2. Materials and methods

2.1. Template preparation

Vertical convective self-assembly was utilized to produce colloidal crystal templates for ALD infiltration and formation of inverse opals after burn-out. Monodisperse polystyrene (PS) particles with a diameter of 762 ± 22 nm (Microparticles GmbH) were diluted in deionized water (diH_2O) to a concentration of 1.0 mg ml^{-1} and assembled onto sapphire substrates (<1-102 >, Crystec GmbH). Substrates were thoroughly cleaned by immersion in 1 wt.% solution of alkaline detergent (Mucasol, Brand, Merz Hygiene GmbH) in diH_2O and sonication for one hour, succeeded by brushing, rinsing (diH_2O), and drying with nitrogen gas. The substrates were additionally cleaned and activated by O_2 plasma treatment for 20 min (Polaron PT7160, Quorum Technologies) right before immersion into the PS-water suspension. The substrates were mounted into the suspension vertically with a small inclination (~8−10°) and the plasma treated surface facing upwards. The colloidal crystals were grown inside a humidity chamber (Memmert HCP 108), at 70 % RH and 55 °C for 90−144 h depending on the substrate area.

2.2. ALD infiltration

The polymeric templates were subsequently infiltrated by ALD in a Savannah™ 100 reactor (Veeco-Cambridge Nanotech), with varying ZrO_2:Al_2O_3 ratios in very-low-temperature super-cycles performed at 95 °C (Fig. 1b) . The precursors used were trimethylaluminum (TMA, min. 98 %, Strem chemicals) and deionized water (diH_2O) for the Al_2O_3 internal loop of the super-cycle, and tetrakis(ethylmethylamino)zirconium (IV) (TEMAZ, 99 %, Strem chemicals – heated to 80 °C) and diH_2O for the ZrO_2 internal loop.

Four types of samples were produced: undoped ZrO_2, doped ZrO_2, dual-layer nanolaminate, and multi-nanolaminate ZrO_2-Al_2O_3 structures (Fig. 1a). The choice for specific aluminum oxide contents and film thicknesses is based on earlier reports regarding ALD multilayered structures as well as investigations regarding aluminum oxide introduction into several systems by methods discussed in the introduction. In this work, we target both the phase stabilization and thermal stability of macroporous structures. The introduction of small contents of aluminum oxide into zirconia structures is capable of stabilizing the tetragonal phase and often praised in sol-gel routes, but investigations in powder metallurgy systems have demonstrated that small amounts of aluminum oxide (here referred to as doping) actually enhance sintering of zirconia compacts, which has also been reported by O'Toole *et al.* in a recent work on ALD-based aluminum oxide doping of YSZ powders. That is why the contents explored in this work are above 25 wt.% and focusing onto composites rather than purely doped structures, to avoid undesired sintering effects. Note, the doped structure with 1 wt.% of Al_2O_3 was produced to elucidate this difference. Further, the nanostructuring is based on two reasons. First, functionally graded structures (FGM) are well known and explored in powder metallurgy systems, as a mean to improve the mechanical properties of composites [55], which could be beneficial to our samples, since cracks are known to nucleate and propagate in our systems upon thermal exposure [12] and thus, FGM structures could arrest such cracks. Secondly, earlier reports about sputtered layered-films by Gajdardziska-Josifovska group [37–40] (discussed in the introduction) as well as PLD films by Ghosh *et al.* [35] and Balakrishnan *et al.*[36] have demonstrated that the layer thickness has a major influence in the crystallite size and phases formed upon thermal exposure.

2.3. Heat treatments

After infiltration, the template was burned out in a muffle oven in air at 500 °C for 1 h (heating rate of 0.8 °C min^{-1}) resulting in an inverse opal macroporous structure. They were further heat treated in a tubular resistive oven also in air with a heating rate of 5 °C min^{-1}. Two consecutive annealing cycles at 1000 °C with 1 h dwell time and at 1200 °C with 2 h dwell time were carried out.

2.4. Characterization

The refractive index and the thickness of the ALD films were measured by spectral ellipsometry (SENProTM, SENTECH Instruments GmbH) on a Si reference wafer placed close to the opals in the ALD cycle. For analysis the data was fitted with a Cauchy model. The IO macroporous' structures were characterized before and after heat treatments, described above. X-Ray diffraction analysis was performed in grazing incidence mode [60,61] for phase identification (Bruker AXS D8 Advance, Cu Kα, 40 kV, 40 mA, step size 0.01°, step time 3 s, incident angle 3°) and estimation of phases' fraction in a semi-quantitative analysis performed using the commercial software DIFFRAC.EVA (Bruker, v 5.1.0.5, database ICDD PDF 2-2020). Electron scanning microscopy (SEM, Zeiss Supra 55 V P) was used to analyze the structural morphology of the inverse opals in both top view and cross section. Images were taken with SE2 detector at an acceleration voltage of 2 kV, aperture of 10 μm, and working distance of 5–6 mm. Scanning transmission electron microscope (STEM) imaging in high-angle annular dark-field (HAADF) mode as well as energy dispersive X-Ray spectroscopy (EDS) spectral imaging was performed using a FEI/Thermo Fisher

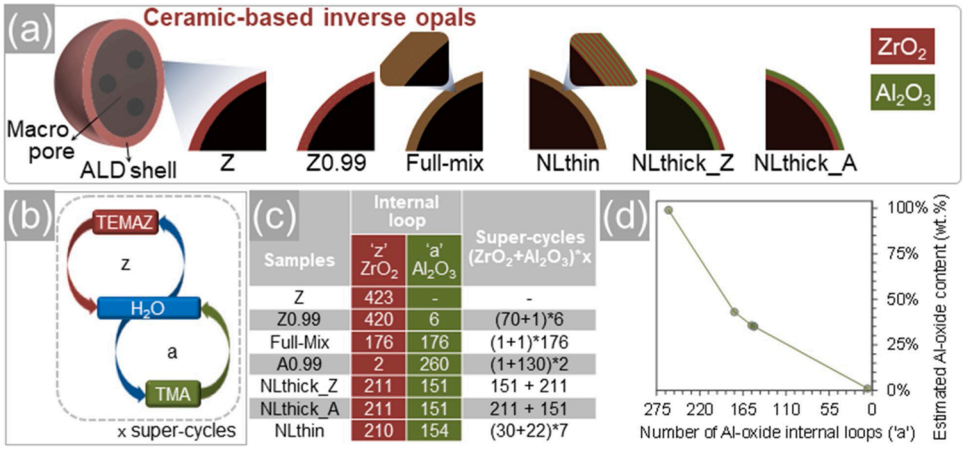

Fig. 1. (a) Schematic drawing showing the nanoscale differences between the samples produced within this study. The schematic represents a 3D view of one macropore, where the black color represents the air, and a 2D zoomed view of the ALD shell, where red color represents zirconia and green color represents alumina. (b) Graphical representation and (c) summary of the ALD super-cycles used for depositing ZrO_2:Al_2O_3 films and infiltrating the colloidal templates to generate the inverse opal macroporous structures. (d) Estimated Al_2O_3 content according to the ratio between 'a' and 'z' internal loops based on the binary processes. Z = zirconia, A = alumina, NL = nanolaminates, NLthick = 25 nm nanolaminates, NLthin = 4 nm nanolaminates (For interpretation of the references to colour in this figure legend, the reader is referred to the web version of this article.).

Scientific Talos F200X equipped with a FEI Super-X G2 EDS detector operating at an acceleration voltage of 200 kV and beam current of 1 nA. Specular reflectance was measured in the wavelength range of 700−2000 nm using a Perkin-Elmer UV/VIS/NIR Lambda 1050 spectrometer.

3. Results and discussion

3.1. Phase formation and evolution

After ALD and burn-out at 500 °C, the majority of the IOs shows crystallization into tetragonal zirconia, with traces of monoclinic phase and no aluminum oxide phases (Fig. 2a), which is in agreement with earlier studies of undoped Al_2O_3 IOs, still amorphous at this temperature [13]. According to the ZrO_2 phase diagram [62,63], only the monoclinic phase (m-ZrO_2) is to be expected in bulk zirconia, composition corresponding to the undoped sample Z, however, the tetragonal phase (t-ZrO_2) is predominant in this sample and all others, doped and nanolaminate ones. This initial transition into a metastable tetragonal phase is well known for crystallization of sol-gel derived amorphous zirconia and it is attributed to the fact that the amorphous phase presents more similarities in regard to the short-range order and local coordination environment to the tetragonal phase than the monoclinic polymorph, thereby the crystallization into this metastable phase is favored [64–66]. Moreover, the presence of broad peaks is an additional indication for the presence of nanocrystalline structures. An earlier work by Shukla *et al.* [22] has also reported a stabilization of the tetragonal phase in nanometric powders. At such, there is an inversion in the common phase transition upon heating from m→t to t→m, which is also observed in our work (Fig. 2b), particularly for the undoped and 1 wt.% Al_2O_3-doped sample. Such inversion in the phase stability, was correlated to the powders surface energy and the different particles size and phases [21, 22]. For such, there is a crossover between the surface enthalpies, assessed by melt solution calorimetry, and the particle sizes resulting in a higher stability of amorphous structures for particle sizes below 10 nm and of the tetragonal phase for sizes between 10–40 nm [21].

Interestingly, the samples with higher compositional mixing, namely the multi-nanolaminates and the Full-Mix samples, show the presence of only tetragonal phase or are still amorphous after burn-out, respectively. This difference indicates that the nanolayering, i.e. alternating supercycling of ZrO_2 and Al_2O_3 layers, further altered the crystallization behavior, as expected. These results agree with what was previously reported for planar nanolayered films produced by sputtering and pulsed laser deposition, which also presented inhibited crystallization and suppression of crystallite growth [35–40]. The authors report a critical thickness for stabilization of the tetragonal phase in zirconia planar thin films, which varies from 10 to 20 nm depending on the deposition process. In this work, the layer thicknesses are 4 nm and 25 nm for the multi-nanolaminates and dual-nanolaminates, respectively, while a homogeneous mix is obtained for the Full-Mix sample. The stabilization is kept even after further heat treatments at 1000 °C (Fig. 2b) and 1200 °C (Fig. 2c) and is more pronounced for the samples with thinner layers.

After heat treatment at 1000 °C for 2 h (Fig. 2b), the undoped and the 1 wt.% Al_2O_3-doped zirconia IOs underwent an extensive phase transformation to m-ZrO_2, which is in agreement with studies on nanostructured sol-gel-based and CVS-based zirconia and expected to happen at temperatures between 600−800 °C. In this sense, the small aluminum oxide doping amount of 1 wt.% has a minor influence in the phases formed after heat treatment at 1000 °C or 1200 °C (Fig. 2c), as both diffractograms and the phase fractions after 1200 °C are similar. This fact is also in agreement with earlier studies on samples with low-doping Al_2O_3 content [29,30], i.e. that the doping only exerts a major influence on the phases formed at higher doping content. Nonetheless, the diffractogram for the undoped sample clearly presents sharper peaks than the 1 wt.% doped one (see Fig. S1a), indicating a crystallite growth inhibition, later discussed.

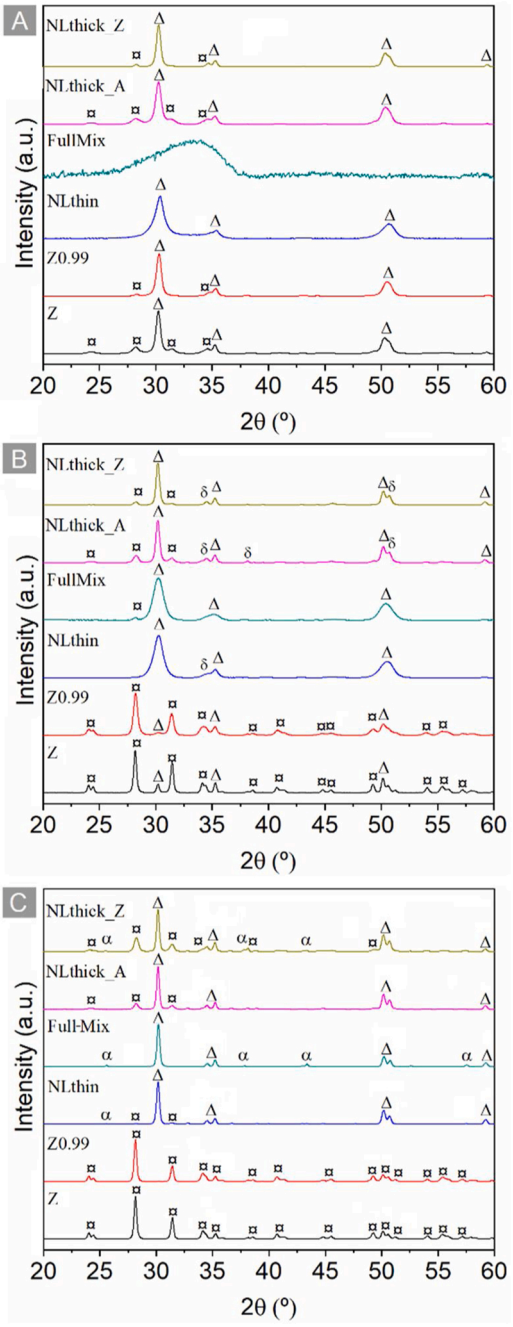

Fig. 2. XRD spectra of undoped ZrO_2, Al_2O_3-doped ZrO_2 and ZrO_2-Al_2O_3 dual and multi-nanolaminates inverse opals after (a) ALD and burn-out and heat treatment at (b) 1000 °C or (c) 1200 °C for 2 h. The symbols indicate (Δ) tetragonal zirconia PDF pattern number 01-080-0784; (¤) monoclinic zirconia PDF pattern number 01-083-0942, (δ) δ^*-Al_2O_3 PDF pattern number 00-046-1215 and (α) α-Al_2O_3 PDF pattern number 00-010-0173.

For the samples with higher Al_2O_3 contents (35−43 wt.%), no extensive tetragonal to monoclinic transition is observed or in other words, the tetragonal phase is stabilized. The Full-Mix IO crystallizes into t-ZrO_2, similar to the NLthin sample after burn-out, while also presenting a peak corresponding to the monoclinic phase. The dual-nanolaminates samples with layer thicknesses of 25 nm also present peaks related to δ-Al_2O_3 phase (zoomed version available in Fig. S1b), which is expected at such temperature [13,67]. The results of the macroporous structures heated up to 1000 °C point out to two stabilization mechanisms acting concomitantly: nanosized structures, defined

by ~50 nm IOs shells, and the introduction of Al^{+3} cations in the ZrO_2 crystal structure, defined by the aluminum oxide content. Since all the macroporous structures present nanometric features, it is no surprise that the tetragonal phase stabilization is more pronounced, i.e. higher fraction of tetragonal phase is present, in IOs with more alumina. This is associated to both introduction of Al^{3+} cations in the ZrO_2 structure, which induces the generation of oxygen vacancies, as well as the generation of Al-O-Al units [68] and even Al_2O_3 clusters [44] as the doping content increases, which generates stresses within crystal the lattices and IOs-shells, also reported to influence the phase transition [21,22,44]. The third mechanism, nanostructuring, becomes relevant at higher temperatures and is discussed in the following paragraph.

After heat treatment at 1200 °C for 2 h, the peaks of the XRD spectra are sharper, indicating further crystallite growth (compare Fig. 2b with 2 c) which is supported by the SEM analysis and TEM grain size analysis (Fig. 5g). Note, the XRD analysis gives information about crystallites, while the SEM images show grains, which can be comprised by one or several crystallites. Most of the peaks related to the zirconia tetragonal phase (PDF pattern number 01−080-0784) could also be assigned to alumina-zirconia mixed oxide (PDF pattern number 00−053-0294), previously reported by Balmer *et al.* [68,69] as a single-phase supersaturated solid solution for liquid-precursor-based spray pyrolyzed powders up to 45 wt.% alumina. A clear distinction between both phases is not possible by XRD. The high-resolution analysis by TEM (Fig. 3) confirmed, however, the presence of a dual-phase microstructure of aluminum oxide and zirconium oxide for all nanolaminates samples, as well as the Full-Mix. A closer look in the element distribution maps reveals a higher homogeneity, regarding the phases' volumetric distribution, for the Full-Mix and the multi-nanolaminates sample than for the dual-nanolaminates. Most samples also show the presence of α-Al_2O_3 peaks in their diffractograms (see zoomed version in Fig. S1c), resembling earlier studies with undoped Al_2O_3 [13] and mullite-coated Al_2O_3 IOs [14], hence expected at these temperatures. Nonetheless, the reason why this phase is not present in the XRD diffractograms of the dual-nanolaminate with alumina outer layer (NLthick_A) is intriguing, especially because a clear phase separation is identified in the SEM images (Fig. 6d). A closer look in the zoomed graph, however (Fig. S1d) reveals peaks corresponding to δ-Al2O3 phase, indicating that the presence of zirconia in this case has delayed the common aluminum oxide phase transitions, which is also reported for sol-gel based 1 mol.% Zr-doped aluminum oxide powders [49].

Moreover, while the undoped and the 1 wt.% Al_2O_3-doped ZrO_2 sample present a full transition to the monoclinic phase, the Full-Mix and nanolaminates IOs present a stabilization of the tetragonal phase. Such restriction and delay of phase transitions has been previously associated to a physical constraint caused by the mismatch between the elastic moduli of Al_2O_3 and ZrO_2. In this case, the higher elastic modulus and stiffness of Al_2O_3 has been demonstrated as beneficial for tetragonal to monoclinic (t→m) ZrO_2 phase transformation suppression [70]. For such samples, the expansion of the zirconia layer or zirconia grains during t→m transition could be physically hindered by the Al_2O_3 layer or by surrounding Al_2O_3 grains, as previously reported for PM-based YSZ [44]. Such effect is enhanced in the Full-Mix and NLthin samples, as these samples are comprised by several nanoclusters or nanolayers. Further, for the nanolaminates case, there is a thermal mismatch between layers upon heating, inducing stress build up, which could further hinder the phase transition [70,71]. Moreover, for the specific case of the multi-nanolaminates, a hindering of the crystallite growth is expected, as once reported for PLD-based and sputtered films. Schofield *et al.* [39] has reported a predicted critical crystallite size of 6.2 nm for the occurrence of the tetragonal to monoclinic phase transition, and suppressed transition for sputtered zirconia layer thickness ≤5 nm. This value is close to the value of 7 nm reported by Ghosh *et al.* [35] for PLD-based planar films. In this work, the layer thicknesses of the NLthin and Full-Mix samples are 4 nm and ≈0.15 nm, respectively. Meanwhile, the dual-nanolaminate samples have a single layer thickness of 25 nm. This explains why, for the dual-nanolaminates samples, peaks corresponding to the monoclinic phase are observed, meaning that while the tetragonal phase was stabilized, part of the shells transformed to monoclinic. A full stabilization is achieved for the Full-Mix sample, although a grain size of 66.9 ± 6.4 nm (Fig. 5g) is achieved after heat treatment at 1200 °C. Meanwhile, NLthin presents traces of the monoclinic phase, even though the layer thickness after deposition is below the previously-reported critical sizes. This is associated to sintering among the layers [38,39], with formation of ZrO_2 grains with sizes above the critical one [35]. For this sample a final average grain size of 92.9 ± 7.4 nm is reached, higher than in the Full-Mix sample.

Furthermore, for the dual-nanolaminates samples, the surface area in contact with air exposure during heat treatment (outer layer) is different between the two types of dual-nanolaminates sample, NLthick_A and NLthick_Z, with the outer layer being directly exposed to the surrounding atmosphere during heat treatment. This difference of material at the interface could influence the balance of oxygen vacancies within the layers, affecting then diffusion [22]. If this hypothesis holds true, the sample with the zirconia outer layer would present less oxygen vacancies and thereby, a lower stability of the tetragonal phase. The hypothesis is supported by the XRD phase fraction semi-quantitative analysis, which shows a higher fraction of monoclinic phase (in relation to the tetragonal phase) for the sample with the Al_2O_3 outer layer than the sample with ZrO_2 outer layer. This effect results in different nanostructures, depicted in Fig. 3. Although both the Full-Mix and the nanolaminates samples present a phase separation, showing alumina and zirconia phase grains, how these phases are distributed within the shell differs. While the Full-Mix and multi-nanolaminates samples present a very homogeneous distribution of the phases, the dual-nanolaminates show a separation of zirconia (red color, Fig. 3e) or alumina (green color, Fig. 3f) at the outer shell area. This is especially pronounced for the sample with the zirconia outer layer, as visualized in the left bottom panel of Fig. 3e.

In summary, for the dual and multi-nanolaminates samples as well as the Full-Mix samples the tetragonal phase is stabilized even after heat treatment at 1200 °C, which is a remarkable result when compared to previous reports of both sol-gel and PM-based structures [28–34]. Structures with similar doping content of ~35−40 wt.% produced by sol-gel processes have shown stability of the tetragonal phase up to 800 °C [30], while a value of 1100 °C is reported for PM-structures fabricated with 28 wt.% alumina-doped zirconia CVS-synthesized powders [29]. In the case of planar films, a value of 1000 °C is reported for multilayered structures with 5x(5/40) nm thickness (zirconia/alumina) for PLD-based films [36] and 1100 °C for 10.5/5 nm (zirconia/alumina) ≈2 μm-thick [42] and 30-4/8 nm ≈3.3 μm-thick sputtered films [41]. These former results on planar films corroborates the importance of the nanolayering, i.e. nanostructuring for the tetragonal phase stabilization. Note, however, sputtering and PLD processes run often at much higher temperatures (> 300 °C at least) than the ALD processes developed within this work (95 °C), demonstrating one of the advantages of using ALD over other process, which enables in this case films deposition onto a wide range of temperature-sensitive substrates. The tetragonal phase stabilization in the IOs is associated to a considerably reduced densification and grain growth when compared to the undoped zirconia, as observed in the SEM analysis (Fig. 5).

3.2. Structural stability upon annealing

In general, all IOs produced by ALD show the typical appearance of ordered colloidal crystals, showing the <111> plane comprised by ALD-shells in SEM top view after the template burn-out (Fig. S2). Upon heat treatment, the doping and nanolaminates structure clearly have an effect on the morphological stability of the inverse opals, showing an improvement in relation to the undoped sample (Figs. 4 and 5). Delamination is not observed in any sample, indicating a strong bonding between the individual material layers, expected for ALD-based

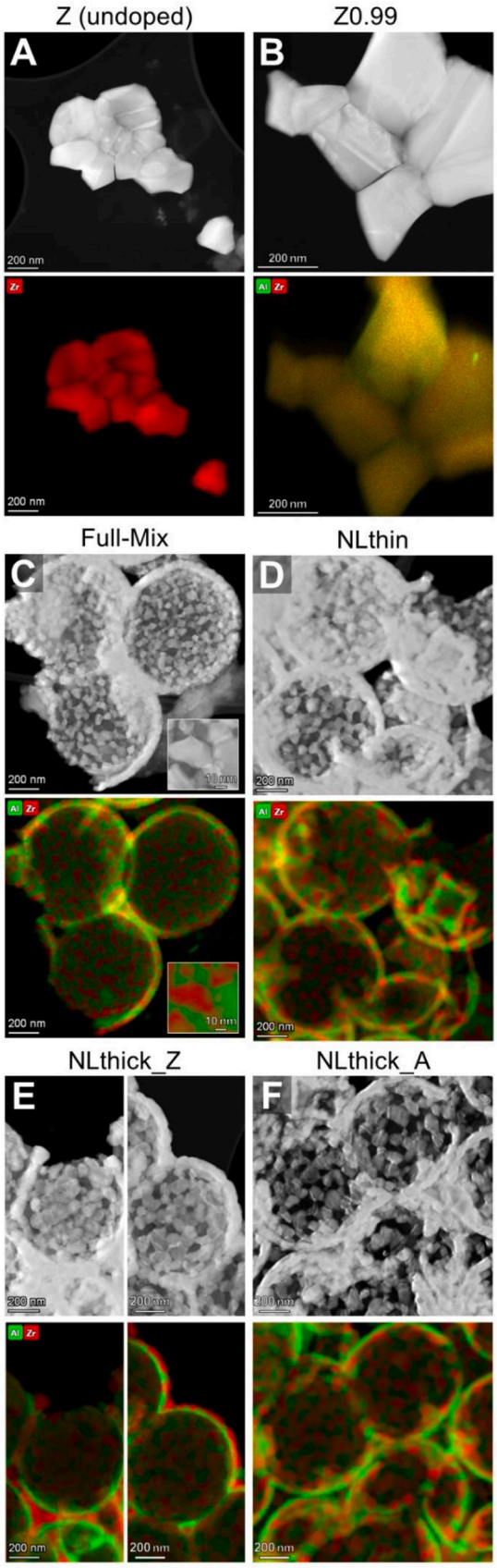

(caption on next column)

Fig. 3. High-resolution TEM micrographs of (a) undoped, (b,c) Al_2O_3-doped ZrO_2 and (d-f) ZrO_2-Al_2O_3 dual and multi-nanolaminates inverse opals. The upper layer shows HAADF images, while the bottom layer shows HAADF-EDS color mapping analysis of the elements Al (green color) and Zr (red color). Intensity in the images are calculated from the background corrected intensities of the k-alpha energies of the elements (Al 1.49 keV and Zr 15.75 keV). The mapping of the element oxygen is hidden to enhance visibility of the relevant elements. The inset in (c) highlights a zirconia grain surrounded by alumina clusters (For interpretation of the references to colour in this figure legend, the reader is referred to the web version of this article.).

structures. While pure zirconia shows visible, smaller grains and a rough surface after heat treatment at 1000 °C for 2 h (Fig. 4a), doped and nanolaminated IOs are smoother and display no large observable grains. Between the nanolaminates, the sample produced with 4 nm multi-nanolaminates (NLthin) and the Full-Mix present a very smooth surface, while the dual-nanolaminates samples displays a slightly rougher surface, comparable to pure zirconia after burn-out (Fig. S2a). Even the smallest investigated aluminum oxide doping of 1 wt.% (sample Z0.99) alters the sintering behavior of the structures and, compared to the non-doped sample (Z), presents slightly smaller grains after heat treatment at 1000 °C as observed in the SEM images of Fig. 4a–b, suggesting a grain boundary pinning effect promoted by the Al cations. This effect is, nonetheless, overthrow as the heat treatment temperature is raised to 1200 °C (Fig. 5) and the grain size analysis results in very similar average grain sizes of around 130 nm (Fig. 5g).

This result for the low-content doping sample differs from what is reported for densification and sintering of alumina-doped zirconia [29] and also for alumina-doped YSZ [25,72,73] PM-based structures. We associate these differences to the nanometric dimensions and macroporous character of our structures, which shall influence both the phase being crystallized as well as the main diffusion mechanism. It is known that nanometric structures [22] and the aluminum oxide doping [29,74] favor the crystallization of zirconia tetragonal phase over the monoclinic one, previously discussed in the 'Phase formation and evolution' section. Studies on sintering undoped zirconia systems are rather rare, presumably because the phase transition (often around 1100−1200 °C for PM-based systems) overlaps with the sintering temperature, so direct comparison between monoclinic and tetragonal phases sintering for the same exact composition is rather challenging. Nonetheless, a thoroughly study by Kanters *et al.* [75], comparing the sintering of undoped monoclinic zirconia with yttria-stabilized tetragonal zirconia for samples with similar initial porosities and grain sizes, has shown that below 1130 °C the sintering rate for the monoclinic phase is higher than that of the tetragonal phase. An analysis of the phase fractions of both samples after burn-out (Fig. 2a) shows a higher fraction of monoclinic phase for the undoped sample than for the doped one, being thereby, more "sinterable". Nonetheless, the heat treatments of all samples were performed in air and thus, the oxygen vacancies created by the doping may be annihilated during annealing, which was demonstrated to decrease densification of ZrO_2 structures, when compared to vacuum sintering [74]. In the specific case of this work, where synthetic inverse opals are exposed to high-temperatures, being more "sinterable" means that the photonic structure formed by the macropores and the ALD-shell is less stable in the undoped sample than in the doped ones. Conversely, while the lack or lower densification is a problem for conventional processing of zirconia-based ceramics by PM, this feature is seen as an advantage for the inverse opals hence it aids to keep the original macro porous structure, unless it is associated with coarsening and grain growth, as detailed in a former publication [13]. At last, the results obtained in our work are in agreement with the work by Srdic *et al.* [29] in which PM-based structures were fabricated from CVS-synthesized nanopowders. For such, grain growth inhibition is reported already for the lowest studied content of 2.5 wt.% presenting almost half of the size than that of the undoped sample. This reported effect is associated to the initial state of the as-synthesized doped powders, comprised by a

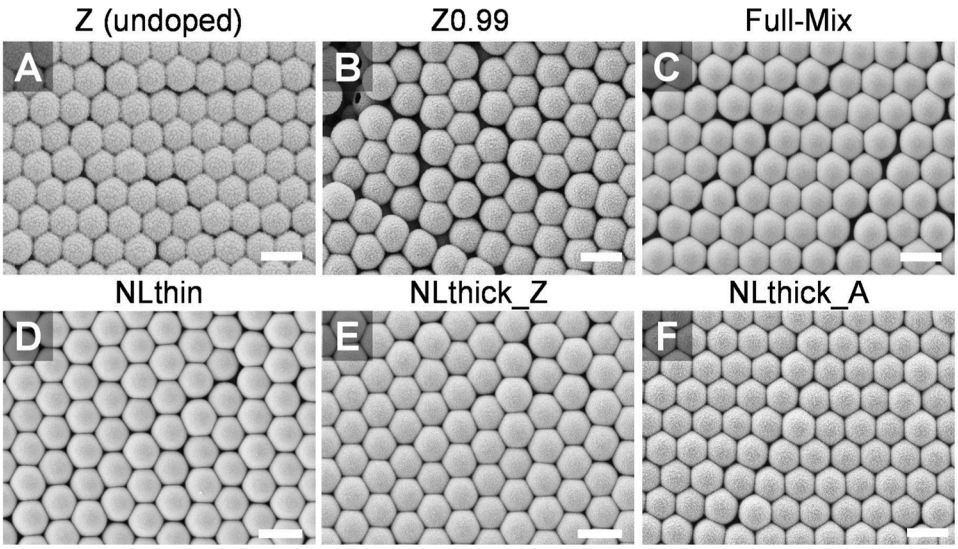

Fig. 4. Comparison between the top view morphology of (a) undoped, (b,c) Al_2O_3-doped ZrO_2 and (d-f) ZrO_2-Al_2O_3 dual and multi-nanolaminates inverse opals imaged by SEM after heat treatment at 1000 °C for 2 h. Scale bars correspond to 1 μm.

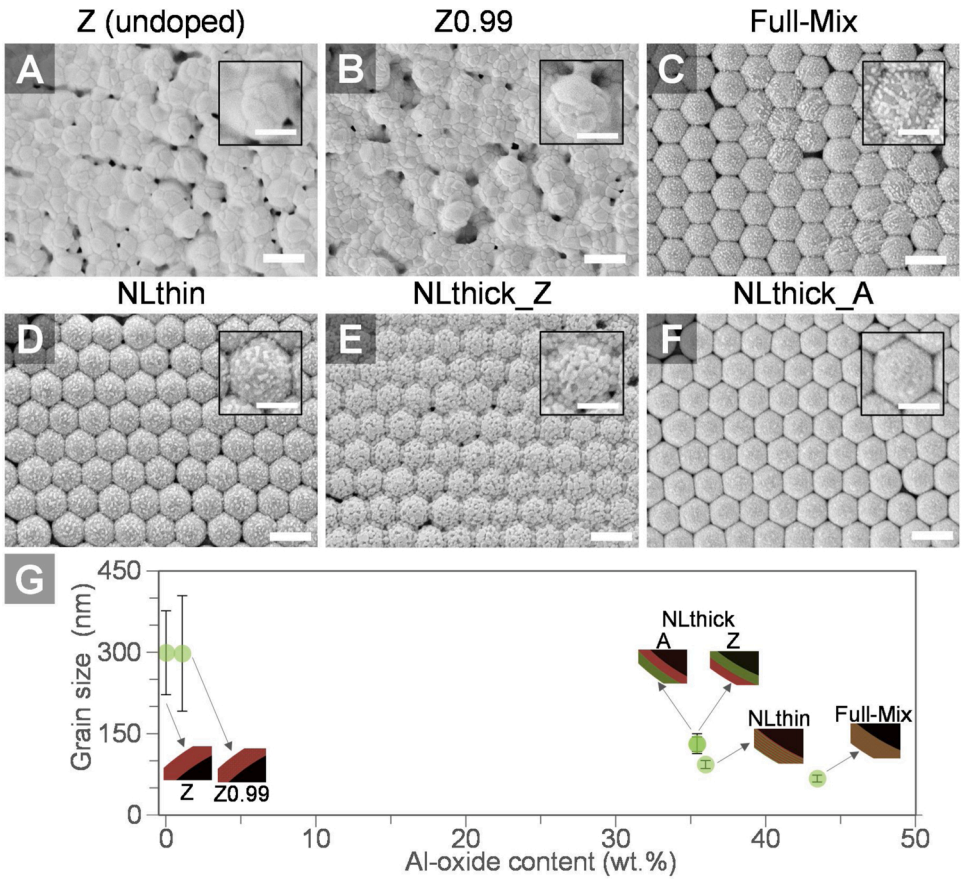

Fig. 5. Comparison between the top view morphology of (a) undoped, (b,c) Al_2O_3-doped ZrO_2 and (d-f) ZrO_2-Al_2O_3 dual and multi-nanolaminates inverse opals imaged by SEM after heat treatment at 1200 °C for 2 h. Scale bars correspond to 1 μm at the main images and 500 nm at the insets. (g) Grain size according to the samples' alumina content and nano-structuring. The schematic drawings inside the graph depict the nanostructuring of the inverse opals' ALD-shells, where black is air, green is alumina and red is zirconia (see Fig. 1 and corresponding text for further details) (For interpretation of the references to colour in this figure legend, the reader is referred to the web version of this article.).

metastable solid solution of two thermodynamically insoluble phases, which segregate in an ultrafine scale upon heating. Such metastable solid solution is also formed for ALD-based Al_2O_3-ZrO_2 planar films with low Al_2O_3 content [76] and also in our doped (Z0.99) IO (see Fig. 3b). The grain size of all samples is displayed in Fig. 5g.

Meanwhile, the results on high-content Al_2O_3 IOs are in agreement with previous reports on both PM-based [29] and sol-gel-based [30] structures. Srdic *et al.* [29] has reported two distinct behaviors during the sintering of 3 and 5 mol.% in comparison to 15 and 30 mol.%. alumina-doped nanocrystalline zirconia. The onset of sintering-induced densification changes from ≈550 °C for undoped and low-content doped zirconia to ≈900 °C for high-content doped zirconia. All works above-mentioned also report a major influence of the alumina doping in the zirconia phase transition, whereas only tetragonal phase is formed at higher doping-content, in contrast to mixed monoclinic/tetragonal phases appearing at the undoped and lower doping-content samples.

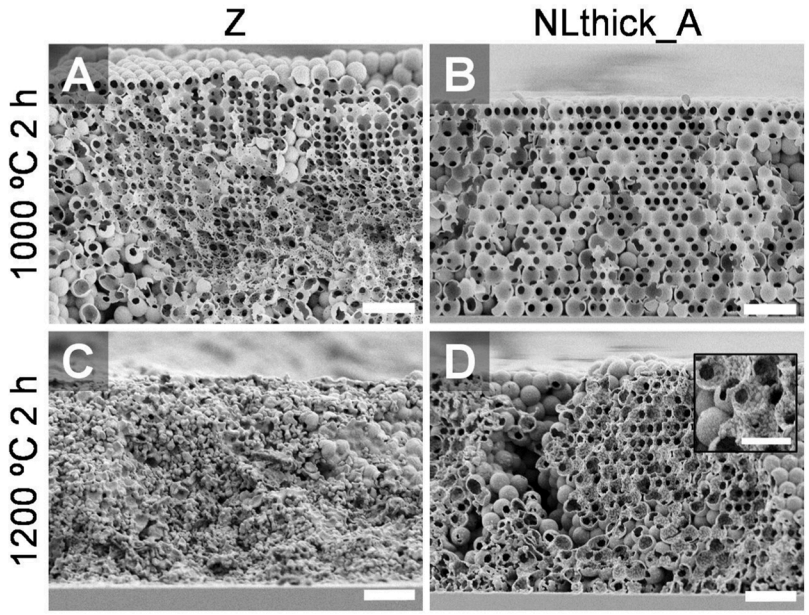

Fig. 6. Cross-sectional view of inverse opals imaged by SEM after heat treatment at (a,b) 1000 °C for 2 h and at (c,d) 1200 °C for 2 h. Inset in (d) highlights the difference between the outer shell (smooth appearance) and inner shell (grains are visible), indicating a phase separation. The debris and different viewing planes in the picture originated during sectioning due to mechanical fracture. Scale bars represent 2 μm at the main images and 500 nm at the inset.

This may also contribute to reduced sintering in high-content doped-structures, as the tetragonal zirconia phase presents a lower sintering rate than the monoclinic one [75]. O'Toole *et al.* [25] has also reported distinct densification behavior depending on the alumina doping content of YSZ powders. The authors showed enhanced densification up to 2.2 wt.% of Al_2O_3, while higher amounts led to opposite effects, such as diffusion and densification hindrance due to introduction of Al_2O_3 into the ZrO_2 lattice, with grain boundary pinning resulting in diffusion barriers for the Zr^{4+} cation. In this case, the location of the dopant has greatly impacted the sintering behavior, impeding neck formation and hindering densification due to the presence of an Al_2O_3 film between adjacent YSZ particles, mostly pronounced in case of films of ~1 nm.

After heat treatment at 1200 °C for 2 h (Fig. 5), both undoped and 1 wt.% Al_2O_3-doped samples reveal extensive sintering with clearly grown necks and destabilization of the ordered inverted opaline structure, whereas all the other samples reveal a higher thermal stability. While the undoped and 1 wt.% Al_2O_3-doped zirconia loses its structural integrity and shows significant grain growth, the nanolaminates sample still presents a stable macroporous structure even after the heat treatment at 1200 °C for 2 h. Similar results were obtained in PM-based bulk structures produced out of Al_2O_3-doped ZrO_2 CVS-synthesized powders by Srdic *et al.* [29]. These differences are highlighted when analyzing the cross-sectional view (Fig. 6) of the IOs. Furthermore, a phase separation become visible at the dual nanolaminate sample, which presents an inner shell with visible grains and a smoother outer shell. Phase separation is also observed for the Full-Mix and NLthin sample. The zirconia-alumina phase diagram [62,63] predicts that such compositions would present a dual phase, as the solid solubility of alumina in zirconia is around 3–4 wt.% [63]. Previous studies by Balmer *et al.* [68,69] have demonstrated, however, the formation of a single-phase supersaturated solid solution for liquid-precursor-based spray pyrolyzed powders up to 45 wt.% alumina. The possible formation of such solid solution is supported by the XRD analysis (Fig. 2c), but not by the TEM one. In this case, the grains visible at the SEM analysis pictured in Fig. 5 are zirconia clusters, whilst the aluminum oxide is a mix of α and δ-Al_2O_3 phases depending on the sample. This is better visualized using TEM analysis and corresponding EDS element mapping shown in Fig. 3. Such phase segregation has also been observed in previous Zr/Al oxide doping reports [29,30]. The differences between these samples is at first surprising, since after heat treatment at 1200 °C for 2 h, one would expect that the IO nanostructure (shell thickness ~50 nm) would be homogenized due to solid state diffusion and thereby all nanolaminates samples, which have alumina contents ranging from 35−43 wt.%, would behave in a similar way. An early study by Ghosh *et al.* [35] have shown, however, that alumina-zirconia (5x(5–15)nm) multi-nanolaminates planar films produced by PLD still present interfaces and phase separation even after heat treatment at 1200 °C, although sintering is observed between the layers, so some of the interfaces are not as sharp as after deposition. The presence of reminiscent layers is also observed in this work, but only for the dual-nanolaminates samples (Fig. 3e–f).

The increased thermal stability obtained in this work is associated to three characteristics, namely, the aluminum oxide content, the phases formed during heat treatment, and the geometrical distribution of ZrO_2 and Al_2O_3 after ALD-infiltration. In this sense, the multi-nanolaminates and the Full-Mix samples, with 35 and 43 wt.% of aluminum oxide, respectively, behave in a quite similar way with regards to phase formation (Fig. 2), phase distribution within the shell (Fig. 3) and overall morphology (Fig. 5). The subtle differences observed in their microstructure arise from the differences in the Al_2O_3 content, as well as the initial distribution of aluminum oxide in the microstructure. For the Full-Mix, a complete homogeneous layer is expected right after ALD, while the multi-nanolaminates' sample present clear boundaries between the alternating ZrO_2 and Al_2O_3 layers [53,56,57]. At the early stages of sintering, the activation energy for diffusion as well as the diffusion paths in these samples are expected to differ, since the Full-Mix already starts from a fully homogenized structure, while the multi-nanolaminates present several clearly defined interfaces between its 14 different layers. This difference in the shell structure promotes different crystallization behavior: at early stages of sintering, the Full-Mix sample is yet amorphous, while the multi-nanolaminates crystallizes into the tetragonal phase (Fig. 2). Interestingly, although the Full-Mix sample shows clustered grains in the SEM analysis, no major secondary phase is identified in the XRD-analysis, but rather a suppression of the typical ZrO_2 phase transformation. Below the clustered-grains, a smooth surface is observed, corresponding to the aluminum oxide phase [13] (see Fig. 3c).

At last, the Full-Mix and multi-nanolaminates samples seems to

display larger grains than the dual-nanolaminate with Al_2O_3 outer shell sample (NLthick_A), but smaller than the ones observed at the dual-layer with ZrO_2 outer shell (NLthick_Z) when observing only the SEM images. The analysis of the grain size by TEM shows, however, that the Full-Mix presents the smaller average grain size (66.9 ± 6.4 nm), followed by the multi-nanolaminates sample (92.9 ± 7.4 nm) and the dual-nanolaminates with alumina (130.3 ± 13.5 nm) and zirconia (131.3 ± 18.3 nm) outer shell. When comparing the dual-nanolaminates' samples, the sample with the Al_2O_3 outer shell presents the least morphological changes after both heat treatments, while the one with the ZrO_2 outer shell displays clear densification and grain growth. This result proves that the initial volumetric distribution of an oxide in relation to one another inside the IO shell plays a major role in sintering and the structural destabilization of IOs, even though the chemical composition and ratio between the oxides is the same for both dual-nanolaminates' samples, accounting to 35 wt.%. In that sense, the nanostructuring promoted by the ALD process is an advantage in relation to former reported routes, such as sol-gel [30–34] or PM-based [28,29] structures because ALD offers the flexibility to design multi stacks and nanolayered structures with a sub-nm level precision [53,54,56,57].

3.3. Optical properties before and after annealing

All IOs presented a photonic band gap before heat treatment in the infrared region between 1200 and 1600 nm (Fig. 7). The refractive indexes of the ALD films, determined by spectroscopic ellipsometry (@632.8 nm), were between 1.85 for the Full-Mix sample and 2.10 for the undoped sample (Z), which is in agreement to previous studies [15,55]. The variation in the main peak position (between 1295 and 1405 nm) is associated to the different compositions between samples, which affects the effective refractive index, but also the nanolaminates structures and their layer thicknesses [77].

After heat treatment at 1200 °C for 2 h, the undoped and 1 wt.% Al_2O_3-doped ZrO_2 samples show the absence of their former photonic band gaps, while all the other samples present photonic band gaps with blue-shifted peaks. The disappearance of the reflection peak is associated with extensive sintering and loss of the opaline structure, discussed in the previous paragraphs and visible in Figs. 5 and 6. The reduction in intensity in the other samples is hypothesized to be related to the opening of microscopic cracks in the IOs structures possibly increasing the transmission component [12,14]. Meanwhile, the blue peak shift is mostly associated to the macropore shrinkage caused by sintering, and the likely changes in n_{eff} caused by diffusion, densification, and phase transformation (discussed in the previous sections) in the IOs shells. In that regard, the dual and multi-nanolaminates samples present a smaller shift in the peak position after heat treatment (~95 nm in average) in comparison to the Full-Mix sample (≈200 nm), once more pointing out to the advantages of nanostructuring.

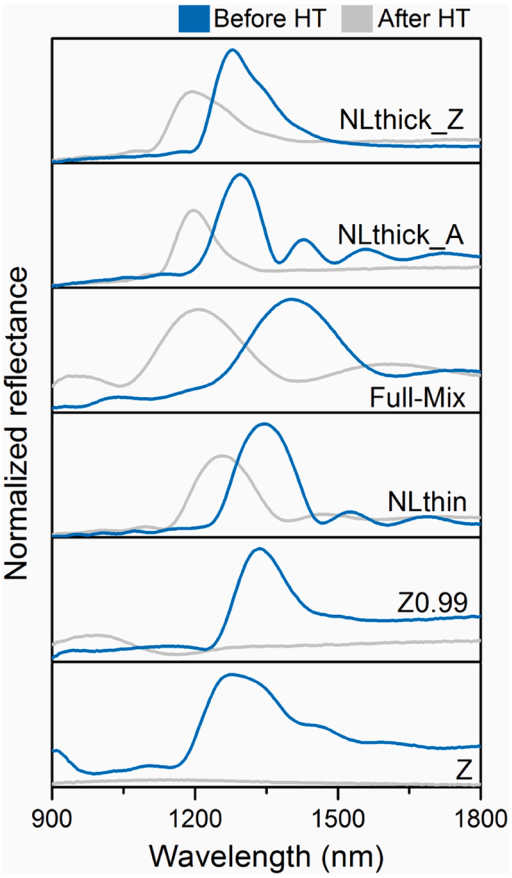

Fig. 7. Reflectance spectra of undoped ZrO_2, Al_2O_3-doped ZrO_2 and ZrO_2-Al_2O_3 dual and multi-nanolaminates inverse opal photonic crystals (blue line) before and (grey line) after subsequent heat treatments at 1000 °C and 1200 °C for 2 h. The spectra were normalized to the maximum value within each graph layer (0–1) to ease the visualization of the differences prior and after heat treatment (For interpretation of the references to colour in this figure legend, the reader is referred to the web version of this article.).

4. Conclusion

Undoped ZrO_2, Al_2O_3-doped ZrO_2 and ZrO_2-Al_2O_3 dual and multi-nanolaminates macroporous structures were successfully fabricated by vertical convective self-assembly followed by infiltration via ALD supercycling. The crystallization of phases and thermal stability was investigated by subsequent heat treatments at 1000 °C and 1200 °C for 2 h. Furthermore, to cover the targeted application as inverse opal photonic crystals (iPhCs), the optical properties of the iPhCs were characterized.

By tailored introduction of Al_2O_3 via ALD, the tetragonal phase was stabilized even after heat treatment at 1200 °C for 2 h for structures produced with very thin alternated ALD ZrO_2-Al_2O_3 multi-layers of ≈4 nm and Full-Mix (1:1 Al_2O_3:ZrO_2 ALD super-cycle) composition. Moreover, we have demonstrated that ALD provides an excellent capability to distribute dopants whilst introducing nano-layering, which further introduces geometrical constraints to disrupt diffusion pathways. Concerning the optical properties, the Full-Mix, dual and multi-nanolaminates iPhCs retained their photonic band gaps even after heat treatment at 1200 °C for 2 h, while the undoped and 1 wt.% Al_2O_3-doped zirconia iPhCs did not. With regard to this, the multi-nanolaminates samples comprised by 4 nm alternated ZrO_2 and Al_2O_3 ALD-layers presented the best optical properties after annealing.

The structures with Al_2O_3 contents ranging from 35 to 43 wt.% showed a substantial increase in their thermal stability, showing inhibited sintering and grain growth in comparison to the undoped and 1 wt.% Al_2O_3-doped structures, enabling its use at high-temperature applications. Such a stabilization is made possible by a combination of factors, namely, the high Al_2O_3 content, the tetragonal phase stabilization, and the nanostructuring, i.e. the geometrical distribution of the ZrO_2 and Al_2O_3 within the macroporous structures.

Acknowledgments

The authors gratefully acknowledge the financial support from the Deutsche Forschungsgemeinschaft(DFG, German Research Foundation) – Projektnummer 192346071 – SFB 986, projects C5, C4, Z3 and C2. Dr. Kaline P. Furlan also gratefully acknowledge Dr. Jonas Sundqvist (Techcet Group LLC and BALD Engineering) for the great scientific discussion regarding ALD of ZrO_2 films and precursors' chemistry.

Appendix A. Supplementary data

Supplementary material related to this article can be found, in the

online version, at doi:https://doi.org/10.1016/j.jeurceramsoc.2021.02.007.

References

[1] K.R. Phillips, G.T. England, S. Sunny, E. Shirman, T. Shirman, N. Vogel, J. Aizenberg, A colloidoscope of colloid-based porous materials and their uses, Chem. Soc. Rev. 45 (2016) 281–322, https://doi.org/10.1039/c5cs00533g.

[2] R.M. Pasquarelli, H.S. Lee, R. Kubrin, R. Zierold, A.Y. Petrov, K. Nielsch, G. A. Schneider, M. Eich, R. Janssen, Enhanced structural and phase stability of titania inverse opals, J. Eur. Ceram. Soc. 35 (2015) 3103–3109, https://doi.org/10.1016/j.jeurceramsoc.2015.04.041.

[3] K.A. Arpin, M.D. Losego, A.N. Cloud, H. Ning, J. Mallek, N.P. Sergeant, L. Zhu, Z. Yu, B. Kalanyan, G.N. Parsons, G.S. Girolami, J.R. Abelson, S. Fan, P.V. Braun, Three-dimensional self-assembled photonic crystals with high temperature stability for thermal emission modification, Nat. Commun. 4 (2013), https://doi.org/10.1038/ncomms3630.

[4] E. Armstrong, C. O'Dwyer, Artificial opal photonic crystals and inverse opal structures - fundamentals and applications from optics to energy storage, J. Mater. Chem. C 3 (2015) 6109–6143, https://doi.org/10.1039/c5tc01083g.

[5] S.G. Rudisill, Z. Wang, A. Stein, Maintaining the structure of templated porous materials for reactive and high-temperature applications, Langmuir 28 (2012) 7310–7324, https://doi.org/10.1021/la300517g.

[6] A. Lashtabeg, J. Drennan, R. Knibbe, J.L. Bradley, G.Q. Lu, Synthesis and characterisation of macroporous Yttria stabilised Zirconia (YSZ) using polystyrene spheres as templates, Microporous Mesoporous Mater. 117 (2009) 395–401, https://doi.org/10.1016/j.micromeso.2008.07.018.

[7] G.I.N. Waterhouse, W.-T. Chen, A. Chan, H. Jin, D. Sun-Waterhouse, B.C.C. Cowie, Structural, optical, and catalytic support properties of γ-Al 2 O 3 inverse opals, J. Phys. Chem. C 119 (2015) 6647–6659, https://doi.org/10.1021/acs.jpcc.5b00437.

[8] S. Sokolov, D. Bell, A. Stein, Preparation and characterization of macroporous α-alumina, J. Am. Ceram. Soc. 86 (2003) 1481–1486, https://doi.org/10.1111/j.1151-2916.2003.tb03500.x.

[9] A. Lashtabeg, J.L. Bradley, G. Vives, J. Drennan, The effects of templating synthesis procedures on the microstructure of Yttria stabilised Zirconia (YSZ) and NiO/YSZ templated thin films, Ceram. Int. 36 (2010) 653–659, https://doi.org/10.1016/j.ceramint.2009.10.009.

[10] R. Kubrin, H.S. Lee, R. Zierold, A.Yu. Petrov, R. Janssen, K. Nielsch, M. Eich, G. A. Schneider, Stacking of ceramic inverse opals with different lattice constants, J. Am. Ceram. Soc. 95 (2012) 2226–2235, https://doi.org/10.1111/j.1551-2916.2012.05156.x.

[11] M. Knez, K. Nielsch, L. Niinistö, Synthesis and surface engineering of complex nanostructures by atomic layer deposition, Adv. Mater. 19 (2007) 3425–3438, https://doi.org/10.1002/adma.200700079.

[12] K.P. Furlan, E. Larsson, A. Diaz, M. Holler, T. Krekeler, M. Ritter, A.Y. Petrov, M. Eich, R. Blick, G.A. Schneider, I. Greving, R. Zierold, R. Janßen, Photonic materials for high-temperature applications: synthesis and characterization by X-ray ptychographic tomography, Appl. Mater. Today. 13 (2018) 359–369, https://doi.org/10.1016/j.apmt.2018.10.002.

[13] K.P. Furlan, R.M. Pasquarelli, T. Krekeler, M. Ritter, R. Zierold, K. Nielsch, G. A. Schneider, R. Janssen, Highly porous α-Al2O3 ceramics obtained by sintering atomic layer deposited inverse opals, Ceram. Int. 43 (2017) 11260–11264, https://doi.org/10.1016/j.ceramint.2017.05.176.

[14] K.P. Furlan, T. Krekeler, M. Ritter, R. Blick, G.A. Schneider, K. Nielsch, R. Zierold, R. Janßen, Low-temperature mullite formation in ternary oxide coatings deposited by ALD for high-temperature applications, Adv. Mater. Interfaces 4 (2017), https://doi.org/10.1002/admi.201700912.

[15] P. Bueno, K.P. Furlan, D. Hotza, R. Janssen, High-temperature stable inverse opal photonic crystals via mullite-sol-gel infiltration of direct photonic crystals, J. Am. Ceram. Soc. 24 (2018) 13146, https://doi.org/10.1111/jace.16012.

[16] J.J. do Rosário, Y. Häntsch, R.M. Pasquarelli, P.N. Dyachenko, E. Vriend, A. Y. Petrov, K.P. Furlan, M. Eich, G.A. Schneider, Advancing the fabrication of YSZ-inverse photonic glasses for broadband omnidirectional reflector films, J. Eur. Ceram. Soc. 39 (2019) 3353–3363, https://doi.org/10.1016/j.jeurceramsoc.2019.04.028.

[17] Y. Jia, C. Duran, Y. Hotta, K. Sato, K. Watari, Macroporous ZrO2 ceramics prepared from colloidally stable nanoparticles building blocks and organic templates, J. Colloid Interface Sci. 291 (2005) 292–295, https://doi.org/10.1016/j.jcis.2005.04.083.

[18] J.J. do Rosário, E.T. Lilleodden, M. Waleczek, R. Kubrin, A.Y. Petrov, P. N. Dyachenko, J.E. Sabisch, K. Nielsch, N. Huber, M. Eich, G.A. Schneider, Self-assembled ultra high strength, ultra stiff mechanical metamaterials based on inverse opals, Adv. Eng. Mater. 17 (2015) 1420–1424, https://doi.org/10.1002/adem.201500118.

[19] F. Tang, T. Uchikoshi, K. Ozawa, Y. Sakka, Effect of polyethylenimine on the dispersion and electrophoretic deposition of nano-sized titania aqueous suspensions, J. Eur. Ceram. Soc. 26 (2006) 1555–1560, https://doi.org/10.1016/j.jeurceramsoc.2005.03.240.

[20] F. Tang, H. Fudouzi, Y. Sakka, Fabrication of macroporous alumina with tailored porosity, J. Am. Ceram. Soc. 86 (2003) 2050–2054, https://doi.org/10.1111/j.1151-2916.2003.tb03607.x.

[21] A. Navrotsky, Thermochemical insights into refractory ceramic materials based on oxides with large tetravalent cations, J. Mater. Chem. 15 (2005) 1883–1890, https://doi.org/10.1039/B417143H.

[22] S. Shukla, S. Seal, Mechanisms of room temperature metastable tetragonal phase stabilisation in zirconia, Int. Mater. Rev. 50 (2005) 45–64, https://doi.org/10.1179/174328005X14267.

[23] S. Vasanthavel, S. Kannan, Structural investigations on the tetragonal to cubic phase transformations in zirconia induced by progressive yttrium additions, J. Phys. Chem. Solids 112 (2018) 100–105, https://doi.org/10.1016/j.jpcs.2017.09.010.

[24] E.S. Lukin, Modern high-density oxide ceramics with controlled microstructure. Part II. Substantiation of the choice of modifying additives that affect the degree of sintering of oxide ceramics, Refract. Ind. Ceram. 37 (1996) 109–119, https://doi.org/10.1007/BF02238719.

[25] R.J. O'Toole, C.J. Bartel, M.U. Kodas, A.J. Horrell, S. Ricote, N.P. Sullivan, C. J. Gump, C.B. Musgrave, A.W. Weimer, Particle atomic layer deposition of alumina for sintering yttria-stabilized cubic zirconia, J. Am. Ceram. Soc. 102 (2019) 2283–2293, https://doi.org/10.1111/jace.16091.

[26] F. Yu, J. Xiao, L. Lei, W. Cai, Y. Zhang, J. Liu, M. Liu, Effects of doping alumina on the electrical and sintering performances of yttrium-stabilized-zirconia, Solid State Ion. 289 (2016) 28–34.

[27] X. Guo, R. Yuan, Roles of alumina in zirconia-based solid electrolyte, J. Mater. Sci. 30 (1995) 923–931, https://doi.org/10.1007/BF01178426.

[28] M.G. Faga, A. Vallée, A. Bellosi, M. Mazzocchi, N.N. Thinh, G. Martra, S. Coluccia, Chemical treatment on alumina–zirconia composites inducing apatite formation with maintained mechanical properties, J. Eur. Ceram. Soc. 32 (2012) 2113–2120, https://doi.org/10.1016/j.jeurceramsoc.2011.12.020.

[29] V.V. Srdić, M. Winterer, H. Hahn, Sintering behavior of nanocrystalline zirconia doped with alumina prepared by chemical vapor synthesis, J. Am. Ceram. Soc. 83 (2000) 1853–1860, https://doi.org/10.1111/j.1151-2916.2000.tb01481.x.

[30] G.T. Dahl, S. Döring, T. Krekeler, R. Janssen, M. Ritter, H. Weller, T. Vossmeyer, Alumina-doped zirconia submicro-particles: synthesis, thermal stability, and microstructural characterization, Materials (Basel) 12 (2019), https://doi.org/10.3390/ma12182856.

[31] M.P. Feth, M. Bauer, G. Kickelbick, O. Metelkina, U. Schubert, H. Bertagnolli, Influence of additives and post-synthesis treatment on the structural properties of sol–gel prepared alumina-doped zirconia studied by EXAFS-spectroscopy and X-ray diffraction, J. Non-Cryst. Solids 351 (2005) 432–443, https://doi.org/10.1016/j.jnoncrysol.2004.12.012.

[32] J. Ortiz-Landeros, M.E. Contreras-García, H. Pfeiffer, Tailored macroporous ZrO2-Al2O3 mixed oxides by template-assisted method: novel materials for catalytic applications, Adv. Tech. Mat. Mat. Proc. J. 9 (2007) 119–124, https://doi.org/10.2240/azojomo0271.

[33] J. Ortiz-Landeros, M.E. Contreras-García, H. Pfeiffer, Synthesis of macroporous ZrO2–Al2O3 mixed oxides with mesoporous walls, using polystyrene spheres as template, J. Porous Mater. 16 (2009) 473–479, https://doi.org/10.1007/s10934-008-9221-z.

[34] O. Metelkina, N. Hüsing, P. Pongratz, U. Schubert, Effects of the post-synthesis treatment on the structural properties of alumina-doped zirconia, J. Non-Cryst. Solids 285 (2001) 64–70, https://doi.org/10.1016/S0022-3093(01)00433-1.

[35] C. Ghosh, D. Ramachandran, G. Balakrishnan, P. Kuppusami, E. Mohandas, HRTEM investigation of phase stability in alumina–zirconia multilayer thin films, Bull. Mater. Sci. 38 (2015) 401–407, https://doi.org/10.1007/s12034-014-0838-z.

[36] G. Balakrishnan, T.N. Sairam, V.R. Reddy, P. Kuppusami, J.I. Song, Microstructure and optical properties of Al2O3/ZrO2 nano multilayer thin films prepared by pulsed laser deposition, Mater. Chem. Phys. 140 (2013) 60–65, https://doi.org/10.1016/j.matchemphys.2013.02.053.

[37] C. Aita, C.M. Scanlan, M. Gajdardziska-Josifovska, Sputter deposited zirconia-alumina nanolaminate coatings, JOM 46 (1994) 40–42, https://doi.org/10.1007/BF03222607.

[38] M. Schofield, C. Aita, P. Rice, M. Gajdardziska-Josifovska, Transmission electron microscopy study of zirconia–alumina nanolaminates grown by reactive sputter deposition. Part II: transformation behavior of tetragonal zirconia nanocrystallites, Thin Solid Films 326 (1998) 117–125, https://doi.org/10.1016/S0040-6090(98)00519-7.

[39] M. Schofield, C. Aita, P. Rice, M. Gajdardziska-Josifovska, Transmission electron microscopy study of zirconia–alumina nanolaminates grown by reactive sputter deposition. Part I: zirconia nanocrystallite growth morphology, Thin Solid Films 326 (1998) 106–116, https://doi.org/10.1016/S0040-6090(98)00542-2.

[40] C.M. Scanlan, M. Gajdardziska-Josifovska, C. Aita, Tetragonal zirconia growth by nanolaminate formation, Appl. Phys. Lett. 64 (1994) 3548–3550, https://doi.org/10.1063/1.111220.

[41] P. Gao, L.J. Meng, M.P. dos Santos, V. Teixeira, M. Andritschky, Study of ZrO2/Al2O3 multilayers, Vacuum 64 (2002) 267–273, https://doi.org/10.1016/S0042-207X(01)00311-6.

[42] H.C. Barshilia, B. Deepthi, K.S. Rajam, Stabilization of tetragonal and cubic phases of ZrO2 in pulsed sputter deposited ZrO2/Al2O3 and ZrO2/Y2O3 nanolayered thin films, J. Appl. Phys. 104 (2008) 113532, https://doi.org/10.1063/1.3040720.

[43] M.H. Maneshian, M.K. Banerjee, Reverse martensitic transformation in alumina–15vol% zirconia nanostructured powder synthesized by high energy ball milling, J. Alloys. Compd. 459 (2008) 531–536, https://doi.org/10.1016/j.jallcom.2007.05.024.

[44] M.H. Bocanegra-Bernal, C. Dominguez-Rios, J. Echeberria, A. Reyes-Rojas, A. Garcia-Reyes, A. Aguilar-Elguezabal, Formation of a protective alumina layer after sintering for the deceleration of low temperature degradation in alumina-toughened zirconia ceramics, Ceram. Int. 42 (2016) 16417–16423, https://doi.org/10.1016/j.ceramint.2016.07.154.

[45] M. Trunec, J. Klimke, Z.J. Shen, Transparent alumina ceramics densified by a combinational approach of spark plasma sintering and hot isostatic pressing,

J. Eur. Ceram. Soc. 36 (2016) 4333–4337, https://doi.org/10.1016/j.jeurceramsoc.2016.06.004.
[46] N. Claussen, Fracture toughness of Al2O3 with an unstabilized ZrO2Dispersed phase, J. Am. Ceram. Soc. 59 (1976) 49–51, https://doi.org/10.1111/j.1151-2916.1976.tb09386.x.
[47] P.K. Rao, P. Jana, M.I. Ahmad, P.K. Roy, Synthesis and characterization of zirconia toughened alumina ceramics prepared by co-precipitation method, Ceram. Int. 45 (2019) 16054–16061, https://doi.org/10.1016/j.ceramint.2019.05.121.
[48] J. Chandradass, J.H. Yoon, D. Bae, Synthesis and characterization of zirconia doped alumina nanopowder by citrate–nitrate process, Mater. Sci. Eng. A 473 (2008) 360–364, https://doi.org/10.1016/j.msea.2007.04.115.
[49] B. Djuricic, S. Pickering, P. Glaude, D. Mcgarry, P. Tambuyser, Thermal stability of transition phases in zirconia doped alumina, J. Mater. Sci. 32 (1997) 589–601, https://doi.org/10.1023/A:1018567230733.
[50] M.W. Zhu, H.B. Ma, P.H. Jin, Y.N. Jin, N. Jia, H. Chen, C.Z. Liu, An insight into the low doping efficiency of Al in sol–gel-derived ZnO:Al films: role of the dopant chemical state, Appl. Phys. A 126 (2020), https://doi.org/10.1007/s00339-020-03670-8.
[51] A.E. Danks, S.R. Hall, Z. Schnepp, The evolution of 'sol–gel' chemistry as a technique for materials synthesis, Mater. Horiz. 3 (2016) 91–112, https://doi.org/10.1039/c5mh00260e.
[52] Sols, gels, and organic chemistry, Ceramic Materials, Springer New York, New York, NY, 2007, pp. 400–411.
[53] P.F. Carcia, R.S. McLean, Z.G. Li, M.H. Reilly, W.J. Marshall, Permeability and corrosion in ZrO2/Al2O3 nanolaminate and Al2O3 thin films grown by atomic layer deposition on polymers, J. Vac. Sci. Technol. A 30 (2012) 41515, https://doi.org/10.1116/1.4729447.
[54] S.-W. Seo, E. Jung, H. Chae, S.M. Cho, Optimization of Al2O3/ZrO2 nanolaminate structure for thin-film encapsulation of OLEDs, Org. Electron. 13 (2012) 2436–2441.
[55] E. Salahi, H. Esfahani, I. Mobasherpour, M.A. Bijarchi, M. Taheri, Sintering behavior and mechanical properties of alumina/zirconia multilayers composite via nano-powder processing, Ceram. Int. 40 (2014) 2717–2722, https://doi.org/10.1016/j.ceramint.2013.10.051.
[56] S. Lee, H. Choi, S. Shin, J. Park, G. Ham, H. Jung, H. Jeon, Permeation barrier properties of an Al2O3/ZrO2 multilayer deposited by remote plasma atomic layer deposition, Curr. Appl. Phys. 14 (2014) 552–557, https://doi.org/10.1016/j.cap.2013.11.053.
[57] J. Oh, S. Shin, J. Park, G. Ham, H. Jeon, Characteristics of Al2O3/ZrO2 laminated films deposited by ozone-based atomic layer deposition for organic device encapsulation, Thin Solid Films 599 (2016) 119–124, https://doi.org/10.1016/j.tsf.2015.12.044.
[58] D.M. Hausmann, E. Kim, J. Becker, R.G. Gordon, Atomic layer deposition of hafnium and zirconium oxides using metal amide precursors, Chem. Mater. 14 (2002) 4350–4358, https://doi.org/10.1021/cm020357x.
[59] J.H. Shim, C.-C. Chao, H. Huang, F.B. Prinz, Atomic layer deposition of yttria-stabilized zirconia for solid oxide fuel cells, Chem. Mater. 19 (2007) 3850–3854, https://doi.org/10.1021/cm070913t.
[60] M. Bouroushian, T. Kosanovic, Characterization of thin films by low incidence X-ray diffraction, Cryst. Struct. Theory Appl 1 (2012) 35–39.
[61] T.C. Huang, P.K. Predecki, in: Presented at DXC on Appl. of X-ray Anal., Denver-USA, 1997.
[62] T. Chraska, K. Neufuss, J. Dubský, P. Ctibor, P. Rohan, Fabrication of bulk nanocrystalline alumina–zirconia materials, Ceram. Int. 34 (2008) 1229–1236, https://doi.org/10.1016/j.ceramint.2007.04.001.
[63] O. Fabrichnaya, F. Aldinger, Assessment of thermodynamic parameters in the system ZrO 2 –Y 2 O 3 –Al 2 O 3, MEKU 95 (2004) 27–39, https://doi.org/10.3139/146.017909.
[64] M. Finsel, M. Hemme, S. Döring, J.S.V. Rüter, G.T. Dahl, T. Krekeler, A. Kornowski, M. Ritter, H. Weller, T. Vossmeyer, Synthesis and thermal stability of ZrO 2 @SiO 2 core–shell submicron particles, RSC Adv. 9 (2019) 26902–26914, https://doi.org/10.1039/C9RA05078G.
[65] J. Widoniak, S. Eiden-Assmann, G. Maret, Synthesis and characterisation of monodisperse zirconia particles, Eur. J. Inorg. Chem. 2005 (2005) 3149–3155, https://doi.org/10.1002/ejic.200401025.
[66] E.W. Leib, U. Vainio, R.M. Pasquarelli, J. Kus, C. Czaschke, N. Walter, R. Janssen, M. Müller, A. Schreyer, H. Weller, T. Vossmeyer, Synthesis and thermal stability of zirconia and yttria-stabilized zirconia microspheres, J. Colloid Interface Sci. 448 (2015) 582–592, https://doi.org/10.1016/j.jcis.2015.02.049.
[67] P.K. Kiyohara, H.S. Santos, A.C.V. Coelho, P.D.S. Santos, Structure, surface area and morphology of aluminas from thermal decomposition of Al(OH)(CH3COO)2 crystals, An. Acad. Bras. Ciênc. 72 (2000) 471–495, https://doi.org/10.1590/S0001-37652000000400003.
[68] M.L. Balmer, H. Eckert, N. Das, F.F. Lange, 27Al nuclear magnetic resonance of glassy and crystalline Zr(1-x)AlxO(2-x/2) materials prepared from solution precursors, J. Am. Ceram. Soc. 79 (1996) 321–326, https://doi.org/10.1111/j.1151-2916.1996.tb08123.x.
[69] M.L. Balmer, F.F. Lange, C.G. Levi, Metastable phase selection and partitioning for Zr(1-x)AlxO(2-x/2) materials synthesized with liquid precursors, J. Am. Ceram. Soc. 77 (1994) 2069–2075, https://doi.org/10.1111/j.1151-2916.1994.tb07098.x.
[70] V. Naglieri, P. Palmero, L. Montanaro, J. Chevalier, Elaboration of alumina-zirconia composites: role of the zirconia content on the microstructure and mechanical properties, Materials 6 (2013) 2090–2102.
[71] R.C. Garvie, Stabilization of the tetragonal structure in zirconia microcrystals, J. Phys. Chem. 82 (1978) 218–224, https://doi.org/10.1021/j100491a016.
[72] G. Suárez, Y. Sakka, Effect of alumina addition on initial sintering of cubic ZrO2 (8YSZ), Ceram. Int. 36 (2010) 879–885, https://doi.org/10.1016/j.ceramint.2009.11.003.
[73] K. Matsui, H. Yoshida, Y. Ikuhara, Review: microstructure-development mechanism during sintering in polycrystalline zirconia, Int. Mater. Rev. 63 (2018) 375–406, https://doi.org/10.1080/09506608.2017.1402424.
[74] V.V. Srdić, M. Winterer, H. Hahn, Sintering behavior of nanocrystalline zirconia prepared by chemical vapor synthesis, J. Am. Ceram. Soc. 83 (2000) 729–736, https://doi.org/10.1111/j.1151-2916.2000.tb01266.x.
[75] J. Kanters, U. Eisele, H. Böder, J. Rödel, Continuum mechanical description of sintering nanocrystalline zirconia, Adv. Eng. Mater. 3 (2001) 158–162, https://doi.org/10.1002/1527-2648(200103)3:3<158:AID-ADEM158>3.0.CO;2-S.
[76] W. Weinreich, L. Wilde, J. Müller, J. Sundqvist, E. Erben, J. Heitmann, M. Lemberger, A.J. Bauer, Structural properties of as deposited and annealed ZrO 2 influenced by atomic layer deposition, substrate, and doping, J. Vac. Sci. Technol. A Vac. Surf. Films 31 (2013), 01A119, https://doi.org/10.1116/1.4765047.
[77] A.A. Chaaya, R. Viter, I. Baleviciute, M. Bechelany, A. Ramanavicius, Z. Gertnere, D. Erts, V. Smyntyna, P. Miele, Tuning optical properties of Al2O3/ZnO nanolaminates synthesized by atomic layer deposition, J. Phys. Chem. C 118 (2014) 3811–3819.